Renewable Energy 256 (2026) 124179

Contents lists available at ScienceDirect

Renewable Energy

journal homepage: www.elsevier.com/locate/renene

Effective H_2 conversion to substitute natural gas on Ni-based catalysts: role of promoters and synthesis method

Antonio Ricca [a], Simona Renda [b,c,*], Christian Di Stasi [d,**], Livia Truda [b], Vincenzo Palma [b]

[a] ENEA – Italian National Agency for New Technologies, Energy and Sustainable Economic Development, Italy
[b] University of Salerno, Department of Industrial Engineering, via Giovanni Paolo II 132, 84084, Fisciano, SA, Italy
[c] Catalysis and Reactor Engineering Group (CREG), Aragon Institute of Engineering Research (I3A), Universidad de Zaragoza, C/ Mariano Esquillor s/n 50018, Zaragoza, Spain
[d] Instituto de Carboquímica (ICB) – CSIC, C/ Miguel Luesma Castán, 4, 50018, Zaragoza, Spain

ARTICLE INFO

Keywords:
CO_2 hydrogenation
Substitute natural gas
Power-to-Gas

ABSTRACT

The methanation of CO_2 is crucial for Power-to-Gas technologies, enabling synthetic natural gas production from renewable sources. Catalyst formulation is key to tuning activity, selectivity, and reaction mechanisms. This study examines CeO_2-ZrO_2-supported catalysts with low Ni loading, evaluating Ru as a promoter. A detailed kinetic analysis clarifies the roles of Ni and Ru in CO_2 hydrogenation, CO methanation, and the reverse water-gas shift (rWGS) reaction. Ni-based catalysts showed high activity for CO and rWGS reactions, with significantly higher rate constants than Ru-based systems. In contrast, Ru was most active for direct CO_2 methanation but had negligible activity for CO methanation, resulting in lower CH_4 selectivity when used alone. Mechanistic studies indicate that Ni promotes a stepwise pathway ($CO_2 \rightarrow CO \rightarrow CH_4$), while Ru facilitates direct CO_2 hydrogenation. Co-impregnation of Ni and Ru enhanced both activity and selectivity, highlighting a synergistic effect. Among all formulations, the sequentially impregnated RuNi/CeZr_TSI catalyst outperformed others. Its success stems from combining Ru strong initial CO_2 activation with Ni high CO methanation ability, leading to greater CO_2 conversion and CH_4 selectivity across a wide temperature range. These results confirm the promise of Ni-Ru/CeO_2-ZrO_2 catalysts for efficient renewable methane production.

1. Introduction

CO_2 hydrogenation is a captivating topic for the technological transition towards green energy. It represents one of the fundamental steps of the power-to-X (PtX) strategy, which allows converting surplus electrical energy from renewable sources into valuable products: green hydrogen through electrolysis, or e-fuels by adding a carbon source [1]. In this context, which carbon source could be better than CO_2 in a sustainability perspective? Among the wide range of hydrocarbons that can be synthesized from CO_2 hydrogenation, methane is the simplest to produce and the most widely consumed [2]. In fact, in the last century natural gas has replaced oil and carbon whenever possible, to the point that, nowadays, it is particularly difficult renouncing to its utilization. Substituting part of the non-renewable natural gas with synthesized methane is a palliative that can help the technological transition until better technologies that avoid CO_2 production will be available or more affordable. Indeed, if not coupled with a CO_2 capture and storage strategy, the methanation reaction cannot be considered as a negative emission technology (NET), [3]. On the other hand, PtX technologies and, in particular, power-to-methane could be integrated in the renewable energies production and supply chain. In fact, it is well-known that power generation from renewable sources is hard to couple with the demand, leading to the need of storage technologies. Batteries can store between 100 kW–10 MW of power and have a relatively short discharge time, while power conversion into chemical energy allows storing up to 500 MW with a higher discharge time [4]. Hence, the surplus renewable electricity (from wind, solar, etc.) could be used to produce H_2 via water hydrolysis which could be combined with captured CO_2 to produce methane. This last step is particularly convenient, when considering that methane can be stored in the existing natural gas infrastructure [5] and employed for a wider variety of purposes. This could also overcome the problems related with the molecular

* Corresponding author. Universidad de Zaragoza, C/ Mariano Esquillor s/n 50018, Zaragoza, Spain.
** Corresponding author. Instituto de Carboquímica (ICB) - CSIC, C/ Miguel Luesma Castán 4, 50018, Zaragoza, Spain.
E-mail addresses: srenda@unizar.es (S. Renda), cdistasi@icb.csic.es (C. Di Stasi).

https://doi.org/10.1016/j.renene.2025.124179
Received 16 April 2025; Received in revised form 3 August 2025; Accepted 4 August 2025
Available online 6 August 2025

H_2 storage and enabling large-scale and long-term storage of renewable energy and facilitating grid balancing [6]. Between 1993 and 2050, about 143 Power-to-Hydrogen or Power-to-Methane projects were completed or planned worldwide, but only 94 remained active by 2022 (56 for H_2 and 38 for CH_4) [7]. Nearly 45 % of these aimed to produce power or heat via grid feed-in, while 43 % focused on syngas and CO_2 methanation, with the rest dedicated to H_2 production and storage. Most projects were located in Europe, especially Germany and Denmark, with Germany leading in capacity (40 MW) [5].

Even though, as aforementioned, hydrogenation of CO_2 to methane can be considered a relatively straightforward process, there is a common denominator in PtX processes: CO_2 is a highly stable molecule with two double bonds, quite difficult to activate. The choice of an appropriate catalyst is vital not only to guarantee a satisfactory reactants conversion but also to ensure to drive the selectivity of the process toward the desired product. At atmospheric pressure and mild temperature (200–400 °C) there are basically two competing reactions: methane synthesis and CO synthesis. Although CO can be further hydrogenated to methane, its stability mines the selectivity of the overall process.

The research of up-to-date formulations have enriched the present literature of a huge number of studies and reviews on the topic [8]. CO_2 methanation occurs through a bifunctional mechanism in which both the support and the active phase play a key role, respectively providing for the activation of carbon dioxide and hydrogen. Supports containing oxygen vacancies (OVs) are particularly suitable, since OVs can split CO_2 in CO* [9]; CeO_2, ZrO_2, In_2O_3 and others belong to this class of compounds. In particular, the doping of CeO_2 with other elements such as Zr, resulted to be beneficial in term of metal dispersion and catalytic stability [10]. Zr^{4+} has a smaller ionic radius than Ce^{4+}, which distorts the ceria lattice and facilitates the generation of oxygen vacancies. These vacancies are crucial for catalytic activity, as they enhance oxygen mobility and improve redox properties. Moderate Zr content (e.g., $Ce_{0.6}Zr_{0.4}O_2$ or $Ce_{0.5}Zr_{0.5}O_2$) often results in the highest concentration of oxygen vacancies and the most favorable catalytic performance [11]. Excessive Zr can lead to structural phases with fewer defects and diminished catalytic activity [12]. For what concerns other promoters, even a very low content of noble metals can significantly enhance the reaction performances on Ni/CeO_2 catalysts [13] and, in particular, the recent work of Tsiotsias et al. highlighted how a loading of 1 wt% of ruthenium in the formulation can remarkably improve the low-temperature activity of the catalyst [14].

Noble metal catalysts, such as those containing ruthenium (Ru), platinum (Pt), or rhodium (Rh), offer significant advantages for the methanation reaction, including higher catalytic activity, improved methane selectivity, and enhanced performance at lower temperatures compared to non-noble metal catalysts. However, the high cost, scarcity, and environmental impact of mining noble metals present challenges for large-scale and sustainable deployment [15]. To align their use with sustainability goals, strategies include minimizing noble metal content by developing bimetallic catalysts (e.g., Ni-noble metal combinations), optimizing catalyst supports to maximize dispersion and activity, and exploring natural sources or recycling of noble metals to reduce environmental impact [16]. Additionally, integrating these catalysts into power-to-gas systems that utilize renewable hydrogen can further enhance the sustainability of the methanation process by enabling carbon-neutral fuel production. Overall, careful catalyst design and resource management are key to leveraging the superior performance of noble metals while addressing economic and environmental concerns.

Nickel is already recognized to be the best non-noble metal to conduct this reaction. From an economic perspective, Ni-based catalysts offer a favorable balance between cost and performance, making them suitable for industrial-scale methanation. While noble metal catalysts can offer higher activity, their higher cost may limit widespread adoption. Therefore, ongoing research into optimizing catalyst formulations, improving durability, and reducing reliance on scarce materials is essential for the economic viability of Power-to-Gas applications.

Another important aspect, when dealing with bimetallic formulation, is the impregnation sequence of the active phases [17]. This aspect could strongly affect the catalytic activity of the material. For example, Ozcan et al. [18] reported that the simultaneous impregnation of the active metals can be beneficial for the catalytic activity, due to the formation of different phases that enhanced the desired reaction.

In this work, we aim to investigate, through experimental and kinetic studies, how the addition of a noble metal (Ru) to a conventional formulation (Ni/CeZr) produces an enhancement in the catalytic performances and change the mechanisms at the basis of this reaction. Considering that different interactions between active species can be driven by different deposition methods, two procedures (two-step impregnation and co-impregnation) were followed. The investigation was firstly carried out by deeply characterizing the different catalytic formulations synthetized. Afterwards, catalytic tests were performed to assess the activity of each catalyst. Finally, after the identification of the most promising formulations, a kinetic model was developed based on one already validated in the literature, to better disclose the effect of the synthesis method on the catalytic performances of different samples.

The results obtained in this study allowed to:

- Identify a valid and active catalytic formulation, highlighting the differences in terms of performances of two different impregnation methods
- Develop a kinetic model which validates and deepens the knowledge on the correlation between metals interactions (associated with the synthesis method) and catalytic activity.

2. Materials and methods

2.1. Catalysts preparation

Four CeZr supported catalysts were studied in this work: monometallic Ni/CeZr and Ru/CeZr and two Ru-Ni bimetallic formulations. Furthermore, to directly compare the performances of Ni/CeZr catalyst with other more conventional formulations, Ni-based catalysts supported onto alumina and ceria were also prepared and tested as benchmark.

Al_2O_3 (commercial, Sasol), CeO_2 (commercial, Rhodia) or CeZr mixed oxide (Ce:Zr = 1:1 M based, commercial, Rhodia) were employed as supports. Preliminary calcination of the supports at 500 °C for 3 h (heating ramp 10 °C/min) allowed to achieve thermal stabilization of morphological and physical properties, and to remove any possibly adsorbed compound.

Nickel or Ruthenium were deposited on the calcined supports through wet impregnation with an aqueous solution of $Ni(NO_3)_2{\cdot}6H_2O$ (Sigma-Aldrich) or $RuCl_3$ (Sigma-Aldrich) in bi-distilled water. The amount of precursor salt was calculated to obtain a nominal loading of 10 wt% and 0.5 wt% of Ni and Ru, respectively. The suspension of the aqueous solution and catalytic support was kept un mixing and heated at 80 °C until complete water evaporation. The samples were dried overnight at 120 °C to eliminate any residual water, and then calcined (500 °C, 3h, 10 °C/min) for the decomposition of the precursor salt and the formation of nickel oxide.

For the bimetallic Ru-Ni samples (nominal loadings 0.5 wt% Ru and 10 wt% Ni), two preparation methods were investigated. A two-steps impregnation (TSI) was performed for the RuNi/CeZr_TSI sample, using the previously calcined Ni/CeZr catalyst for Ru impregnation. On the other hand, co-impregnation (CIM) was employed for the synthesis of the RuNi/CeZr_CIM catalyst. In this case, the ruthenium and nickel were simultaneously deposited onto the support, through a solution of both the precursor salts.

Reduction of all samples was performed in a fixed-bed quartz reactor at 600 °C for 3 h in a N_2/H_2 (90/10 vol%) stream. Once reduced and cooled down to room temperature, the samples underwent passivation with a N_2/O_2 (99/1 vol%) stream for 3 h to avoid uncontrolled oxidation

when exposed to the atmosphere.

2.2. Catalysts characterizations

The specific surface area (SSA) was calculated performing a 5 points N_2-adsorption isotherms at −196 °C with a Sorptometer 1040K (Costech International) and applying the BET equation. Prior to the analysis, the samples were degassed in vacuum at 150 °C for 1 h, to eliminate any impurities from the surface.

X-Ray Power Diffraction (XRD) analysis of reduced samples was performed with a D8 Advance Series 2 diffractometer (Brucker), using a Ni-filtered Cu-Kα radiation source in the 2θ range 10–80° (scan time 3 s, intervals of 0.5°).

The actual metal loading of the catalysts was determined via inductively coupled plasma optical emission spectrometry (ICP-EOS). The samples were firstly digested through sodium peroxide fusion procedure and then introduced into the Spectroblue (AMETEK) for the quantification.

The reducibility properties were evaluated through temperature programmed reduction (TPR), in an AutoChem Analyzer II 2920 (MICROMETRICS®). An amount of 0.2 g for each sample was loaded into the equipment. The catalysts were firstly dried at 105 °C for 1 h in Ar atmosphere to remove the atmospheric moisture and then, after a cooling step, heated up to 700 °C at 5 °C min^{-1} in reducing atmosphere (10 vol% H_2 in Ar).

The number of basic sites was evaluated via CO_2 temperature programmed desorption (CO_2-TPD), in the same equipment employed for the TPR analysis. For the TPD analyses, reduced and passivated samples (0.2 g) were dried under the same conditions of the TPR and then cooled down to 40 °C and exposed to 50 NmL min^{-1} of a mixture of 5 vol% of CO_2 in Ar for 60 min. Then, the remaining physiosorbed CO_2 was purged treating the sample with a pure Ar stream for other 60 min. Finally, the sample was heated up in Ar to 750 °C with a heating ramp of 10 °C min^{-1}.

The Raman spectroscopy technique was employed to investigate the differences between the CeZr support compared to bare ceria. For the analysis, a Micro-Raman Horiba Jobin Yvon HR800UV was employed, using visible radiation (532 nm); the Raman response of the samples was registered in the range 120–2000 cm^{-1}, using a 3 mW laser power. Since Raman spectroscopy is a local analysis, five different points have been considered for the measurements, to ensure the reproducibility of the result.

The samples morphology and elemental distribution were evaluated via SEM microscopy (SEM EDX Hitachi S-3400).

2.3. Experimental setup and procedure

The experiments were conducted in a tubular AISI 316L stainless steel reactor, with a nominal diameter of 12.7 mm (i.d. 10.3, wall thickness 1.2 mm). For each test, 1 g of catalyst (particles diameter in the range of 180–355 μm) was diluted with 500–710 μm quartz spheres, reaching a total volume equal to 2 cm^3. Quartz addition allowed to obtain a suitable catalytic bed length and smooth the temperature increase due to the exothermicity of the reaction. The catalyst was placed in the central zone of the reactor, held by two quartz wool disks. Two K-type thermocouples continuously monitored the gas temperature at the inlet and outlet section of the catalytic bed. The temperature control of the system was assured through an annular electrical furnace with three individual heating zones. A battery of mass flow controllers provided by Bronkhorst fed the reaction mixture to the reactor, while the gas composition was evaluated through a Hiden Analytical mass spectrometer, that provided the volumetric fraction (dry-base) of H_2, CH_4, CO, Ar and CO_2 by observing respectively fragments 2, 15, 28, 40 and 44. Further specification and the experimental setup scheme were previously reported elsewhere [19].

Prior to each experimental test, the calcined catalysts were activated in a 5 % H_2 in Ar stream, raising the temperature with a 5 °C/min heating rate, from room conditions up to 500 °C. For the experiments, the reactants were fed in stoichiometric ratio ($H_2/CO_2 = 4$), and a molar dilution ratio Ar/reactants = 1 was employed to contain the temperature increase. The activity tests were conducted on a temperature ramp, raising the temperature from 200 °C to 450 °C, with a heating rate of 2 °C/min.

The fluid-dynamic conditions were fixed by the space velocity (SV), defined as the ratio between the volumetric flow rate and the catalyst mass. The overall inlet stream (reactants and inert) was considered in the determination of SV, as commonly reported in literature for CO_2 methanation studies. For the chemical support screening, it was adopted a SV = 30 $NL{\cdot}h^{-1}{\cdot}g_{cat}^{-1}$ while, to study the kinetic aspect, the powder samples were stressed with a SV = 60 $NL{\cdot}h^{-1}{\cdot}g_{cat}^{-1}$.

The catalytic performances were evaluated in terms of CO_2 conversion (X_{CO2}), CH_4 yield (Y_{CH4}) and CH_4 selectivity (S). F_i represents the molar flow of the "i" species.

$$X_{CO_2}(\%) = \frac{F_{CO_2,in} - F_{CO_2,out}}{F_{CO_2,in}} \cdot 100 \quad \text{Eq. 1}$$

$$Y_{CH_4}(\%) = \frac{F_{CH_4}}{F_{CO_2,in}} \cdot 100 \quad \text{Eq. 2}$$

$$S(\%) = \frac{F_{CH_4}}{F_{CO_2,in} - F_{CO_2,out}} \cdot 100 \quad \text{Eq. 3}$$

2.4. Mathematical model and kinetics

For the derivation of the kinetic parameters, a literature model was adopted. The most credited equations for representing a CO_2 methanation system were provided by Xu and Froment [20], that used a Langmuir-Hinshelwood based mechanism, considering a single-molecule adsorption/desorption mechanism for each component except water, as given in the expression of DEN^2.

A summary of the equations employed for model is given in Table 1.

Eqs. 4–6 are the considered reaction, respectively CO methanation (r_1), reverse water-gas shift (rWGS, r_2) and CO_2 methanation (r_3). Eqs. 7–10 represent the reaction rates for the three reactions, respectively. Kinetic constants k_i are expressed according to the Arrhenius equation (Eq. 11). Equilibrium constants $K_{eq,i}$ and expressions for the adsorption constant K_j (Eqs. 12–18) were obtained from the literature [21].

Table 1
Equations employed for the kinetic model.

$CO + 3H_2 \leftrightarrows CH_4 + H_2O$	Eq. 4
$CO_2 + H_2 \leftrightarrows CO + H_2O$	Eq. 5
$CO_2 + 4H_2 \leftrightarrows CH_4 + 2H_2O$	Eq. 6
$(-r_1) = \frac{k_1}{p_{H_2}^{2.5}} \cdot \left(p_{CH_4} \cdot p_{H_2O} \cdot \frac{p_{H_2}^3 \cdot p_{CO}}{K_{eq,1}} \right) / (DEN)^2$	Eq. 7
$(-r_2) = \frac{k_2}{p_{H_2}} \cdot \left(p_{CO} \cdot p_{H_2O} \cdot \frac{p_{H_2} \cdot p_{CO_2}}{K_{eq,2}} \right) / (DEN)^2$	Eq. 8
$(-r_3) = \frac{k_3}{p_{H_2}^{3.5}} \cdot \left(p_{CH_4} \cdot p_{H_2O}^2 \cdot \frac{p_{H_2}^4 \cdot p_{CO_2}}{K_{eq,3}} \right) / (DEN)^2$	Eq. 9
$DEN = 1 + K_{CO} \cdot p_{CO} + K_{H_2} \cdot p_{H_2} + K_{CH_4} \cdot p_{CH_4} + K_{H_2O} \cdot p_{H_2O} / p_{H_2}$	Eq. 10
$k_i = k_i^{\circ} \cdot e^{-E_{a,i}/R \cdot T}$	Eq. 11
$K_{eq,1} = 1.198 \times 10^{23} \cdot e^{\frac{-26830}{T}}$ [Pa^2]	Eq. 12
$K_{eq,2} = 1.767 \times 10^{-2} \cdot e^{\frac{4400}{T}}$ [-]	Eq. 13
$K_{eq,3} = K_{eq,1} \cdot K_{eq,2}$	Eq. 14
$K_{CH_4} = 6.65 \times 10^{-9} \cdot e^{\frac{38280}{R \cdot T}}$ [Pa^{-1}]	Eq. 15
$K_{CO} = 8.23 \times 10^{-10} \cdot e^{\frac{70650}{R \cdot T}}$ [Pa^{-1}]	Eq. 16
$K_{H_2} = 6.12 \times 10^{-14} \cdot e^{\frac{82900}{R \cdot T}}$ [Pa^{-1}]	Eq. 17
$K_{H_2O} = 1.77 \times 10^{5} \cdot e^{\frac{-88680}{R \cdot T}}$ [-]	Eq. 18

3. Results and discussion

3.1. Catalysts characterizations

In Table 2 are resumed the results of the chemical composition and the specific surface area analysis. As can be observed, monometallic Ni-based catalysts displayed a SSA remarkably lower than that of the corresponding support, indicating, as expected, the clogging of part of the original porous structure. Ru deposition on CeZr support did not have the same effect, although this is certainly ascribable to the much lower loading of active phase employed. Bimetallic catalysts did not exhibit a notable difference between the two samples, indicating that the preparation method did not significantly impact on the textural properties of the final catalyst. Furthermore, the additional calcination step performed on the TSI sample did not affect the SSA, demonstrating the thermal stability of the catalyst.

ICP analysis gave the weight percentage of the metallic species, in good agreement with the nominal loadings. In addition, it allowed to confirm the 1:1 M ratio of Ce:Zr in the commercial support.

The XRD analysis results are displayed in Fig. 1. Comparing the CeZr spectrum to CeO_2 as a reference, it is possible to see the characteristic shift of CeO_2 peaks when Zr atoms are in the matrix. Furthermore, Ni presence is slightly visible at 44.5° and 51.9°. Both peaks correspond to FCC-centered structure, indicating that Ni is present in a single-phase structure. This was observed for all samples, meaning that nor the addition of a second metal neither the method for its deposition influenced the final crystalline form of nickel. Furthermore, no NiO was detected by XRD, implying that the reduction procedure was adequate. For the bimetallic samples, even though ruthenium loading was confirmed by ICP, it cannot be observed through the XRD spectra, indicating crystallites dimension smaller than the instrument detection limit (3 nm), were likely obtained thanks to the noble metal low loading.

Raman spectroscopy (Fig. 2) was performed on CeO_2 and CeZr support only, to evaluate the role of zirconium in modifying the OVs of the ceria matrix. The CeO_2 support shows the characteristic peak at 462 cm^{-1} (of intensity I_{F2g}), ascribable to the first order F_{2g} mode of ceria, which corresponds to Ce^{4+}-O-Ce^{4+} wagging (≈460 cm^{-1}) [22]. Defects induced bands are visible at 262 and 593 cm^{-1} (≈200 and ≈ 600 cm^{-1} according to Ref. [23]). In particular, the peak at 593 (of intensity I_D) is ascribable to Ce^{3+} atoms in the matrix. Finally, the peak at 1172 cm^{-1} corresponds to the second-order longitudinal modes of cubic CeO_2 fluorite phase [24]. The ratio I_D/I_{F2g} conventionally expresses the number of defects in the structure, and in the case of the employed CeO_2 it can be visually observed that this is not particularly high. Things change in case of the CeZr support. The Raman response of CeZr shows lower-intensity and shifted peaks, compared to CeO_2. Both phenomena, producing a completely different I_D/I_{F2g} ratio, can be related to the increase of disorder into the fluorite structure by the partial substitution of

Table 2
Resume of the prepared catalyst with label and preparation method, XRF, ICP and SSA results.

Name	Preparation method	ICP (wt. %)		SSA_{BET} (m^2/g)	Crystallites size (nm)
		Ni	Ru		Ni
Al_2O_3	calcined	–	–	230	–
CeO_2	calcined	–	–	172	–
CeZr	calcined	–	–	80	–
Ni/Al_2O_3	IM	–	–	161	4.21
Ni/CeO_2	IM	–	–	115	3.59
Ni/CeZr	IM	8.4	–	65	4.78
Ru/CeZr	IM	–	0.4	77	–
RuNi/CeZr_CIM	CIM	8.9	0.5	63	7.35
RuNi/CeZr_TSI	TSI	7.9	0.4	61	8.06

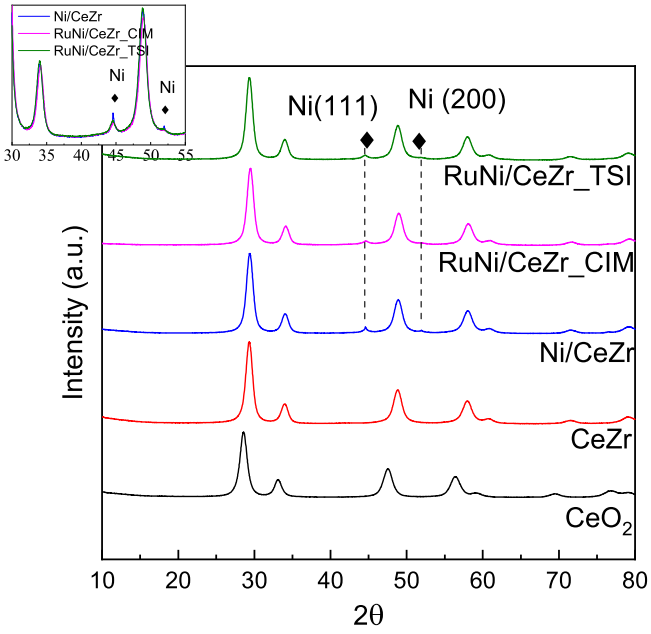

Fig. 1. XRD spectra of selected catalysts and supports samples.

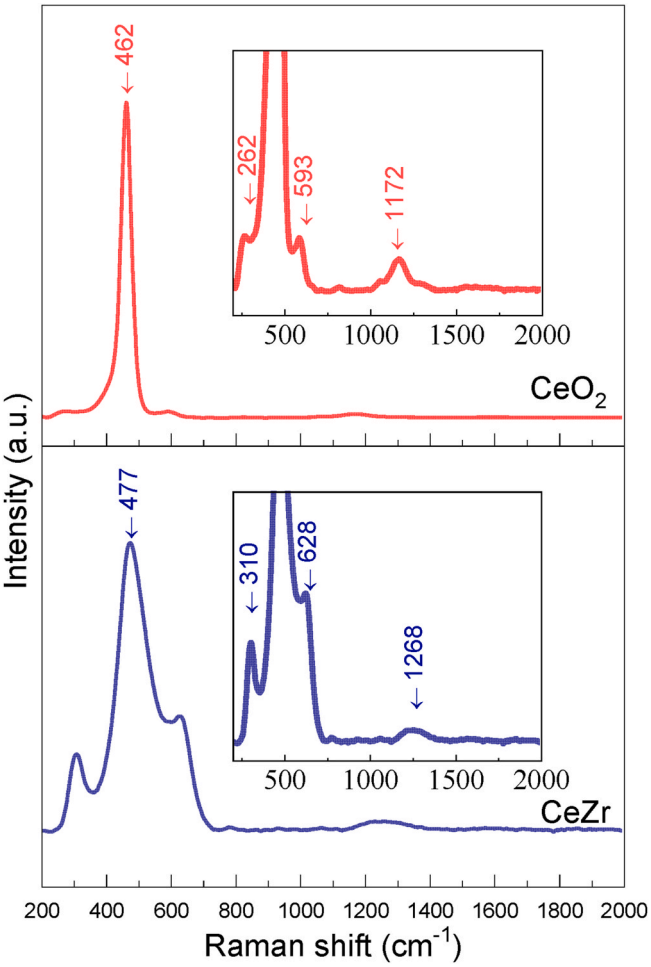

Fig. 2. Raman spectra of the CeO_2 and CeZr.

Ce by Zr and/or existence of oxygen vacancies [25]. The OVs serve primarily for the CO_2 adsorption and activation, hence their presence and amount could be determinant for the reaction; nevertheless, the overall efficiency of a catalyst cannot be determined by this sole parameter.

The TPR analysis results are reported in Fig. and through peaks deconvolution, it was possible to distinguish the contribution of each component. Since CeO_2 reduction properties are well-known and Al_2O_3 is not a reducible support, only the bare CeZr support was characterized through TPR analysis. It was observed that the support is indeed reducible, showing a reduction peak at 490 °C. The three Ni-based monometallic catalysts (Ni/Al_2O_3, Ni/CeO_2, Ni/CeZr) showed remarkably different reducibility properties. It is generally recognized that Ni oxide can exhibit three reduction peaks, that could be addressed as α, β and γ in order of progressive increase in its bond with support. According to the study of Gil-Calvo et el. [26], bulk NiO only shows α reduction peak, while β and γ peaks are observable in bulk $NiAl_2O_4$. As expected, α-NiO reduction peak can be observed in Ni/CeO_2 and Ni/CeZr samples approximately at the same temperature (300 °C), even though the peak is sharper in case of CeO_2 support. On the other hand, Ni/Al_2O_3 sample presented mainly β and γ-NiO, respectively at 560 and 750 °C, indicating that when Ni is supported onto alumina only the nickel aluminate phase – less reactive – is formed. The appearance of this phase is consistent with the calcination temperature, since it is formed when overgoing 400 °C during calcination [27], which is the case of this study. In the case of Ni/CeO_2 sample, the noticeable presence of NiO_x (weakly bonded nickel) is in good agreement with previous literature [28].

In the Ni/CeZr catalyst, the shoulder of the reduction peak in ascribable to support reduction; CeZr reduction is also visible above 300 °C in the Ru/CeZr sample. The low-temperature peaks in Ru/CeZr sample are both to be attributed to ruthenium oxide reduction; contrarily to NiO, where Ni can only pass from Ni^{2+} to Ni^0, ruthenium has multiple (five) oxidation stages. Considering only the most stable phases, the reduction is likely to follow the path Ru^{4+} (RuO_2) > Ru^{2+} (RuO) > Ru^0. In addition, the strong spillover phenomenon produced by the presence of the noble metal can be observed in Ru/CeZr reduction profile.

The bimetallic catalysts showed significant differences in their reducibility, according to the different preparation methods. It worth noting that in the TSI-prepared sample (RuNi/CeZr_TSI), both nickel and ruthenium oxides reduced at the same temperature of the corresponding monometallic samples, suggesting that no significant interaction occurs between the two metals. On the other hand, in the CIM catalyst (RuNi/CeZr_CIM) the reduction of both metals is anticipated at lower temperature; moreover, the second ruthenium reduction peak is particularly wide and intense, suggesting intermediate reduction stages correlated to metals interactions. Surely, spillover occurs in bimetallic catalysts as well, but it was not possible to discern the support reduction through peaks deconvolution.

The TPD analysis (Fig. 4) highlighted the differences between the CeO_2 and CeZr support. According to the conventional interpretation, both supports has mostly weak basic sites. Addition of Ni and Ru seemed to increase CO_2 desorption in the medium-basicity region, suggesting a redistribution of the CO_2 chemisorption sites, supported by the observation of the total amount of desorbed CO_2 ($mmol_{CO2}\ g_{cat}^{-1}$), which did not vary significantly. This could be beneficial for CO_2 methanation since it may be possible to activate earlier the reactant and, consequently, lowering the onset reaction temperature.

SEM-EDX images were obtained for bimetallic catalysts and the Ni/CeZr was used as a reference. The morphology of the catalyst, mainly characterized by spherically shaped particles, can be observed from Fig. 5. In general, Ni appear to be evenly dispersed onto the support surface. Nevertheless, it is worth noting that also SEM-EDX characterization is a local analysis, meaning that the result of the observation can vary point to point. Observing the EDX mapping for the bimetallic catalysts, it can be noted that Ru had a worse dispersion, despite its low loading. In addition, it seems that Ru tends to deposit on Ni sites, and this can be deducted by the images (h) and (j): the space free of Ni particles is not filled in from Ru sites during the second impregnation, while Ru prefers to attach in the proximity of Ni crystallites. This is likely due to the presence of Ni oxide, which is a highly hydrophilic site [29]. The double impregnation step also eliminates the casualty of a portion of the support not wetted by the solution, but indicates a systematic preferential deposition.

3.2. Catalytic tests

Fig. 6 reports the activity and selectivity of Ni/CeZr catalysts compared to benchmark formulations at 30 $NL(hg)^{-1}$. As can be observed, at the investigated space velocity conditions Ni/CeZr catalyst was already active at temperature as low as 250 °C, which is a significant result. In addition, the maximum of CO_2 conversion (80 %) was observed from 260 °C to 320 °C approximately. The Ru/CeZr formulation outperforms the more conventional alumina-supported catalysts and approaches the CO_2 conversion levels typically achieved with CeO_2-supported catalysts, which are recognized as among the best supports for CO_2 methanation. In terms of methane selectivity, the Ni/CeZr sample exhibited nearly unitary selectivity across the entire temperature range, closely approaching equilibrium values as the temperature increased.

The results obtained with the CeO_2 and CeZr supported samples can be ascribed to their unique combination of an elevated oxygen transport capacity coupled with the ability to shift between reduced and oxidized states (i.e., Ce^{3+} – Ce^{4+}) as confirmed by Raman analysis (Fig. 2). This property is well-known to promote CO_2 adsorption and activation [30]. It is noticeable that the ceria-based sample assured a slightly better activity, by both earlier activating the reaction and better approaching the thermodynamic equilibrium conversion than the CeZr supported catalyst. This difference can be related to the higher reducibility (Fig. 3) and higher number of basic sites (Fig. 4) showed by the ceria-supported sample, characteristics which could both promote low-temperature CO_2 activation.

Considered the high activity of the Ni/CeZr sample in the preliminary evaluation, the space velocity was doubled to test the bimetallic formulations (Fig. 7). Comparing the activity of Ni/CeZr with the previous experiments (Fig. 7a vs Fig. 6a), it can be observed that higher temperatures were needed for the activation of the catalyst, and it the equilibrium conversion was approached only above 400 °C. Also, there was an overall drop of methane selectivity value, from almost 100 % to approximately 90 % at its best. Considering the harsh operating conditions, this result was expected. It should be noted that the slight excess of the experimental value over the equilibrium curve at 450 °C is not physically plausible and is likely due to experimental and measurement uncertainties.

The monometallic Ru/CeZr formulation was also tested for sake of comparison. It has been widely reported that, depending on the methanation operating conditions, Ru could be an excellent catalyst. In this case, the low loading of ruthenium cannot cope with the high space velocity employed, leading to the obtainment of a low-active and low-selective catalyst which resulted to be remarkably worse than the monometallic non-noble metal formulation. In addition, ruthenium is known to promote the direct CO_2 methanation, but in this case a significant amount of CO was also observed during reaction, especially at low temperature. This could indicate a competition between the Sabatier reaction and the reverse water-gas shift reaction. According to thermodynamics, methane selectivity should decrease with temperature while CO selectivity should increase, but when a catalyst works far from equilibrium – as in this case – the kinetic aspect becomes more relevant, and the CO_2 methanation could need higher temperature to be significantly activated.

Although the low ruthenium loading alone was insufficient to catalyze CO_2 methanation effectively, its addition to the Ni/CeZr

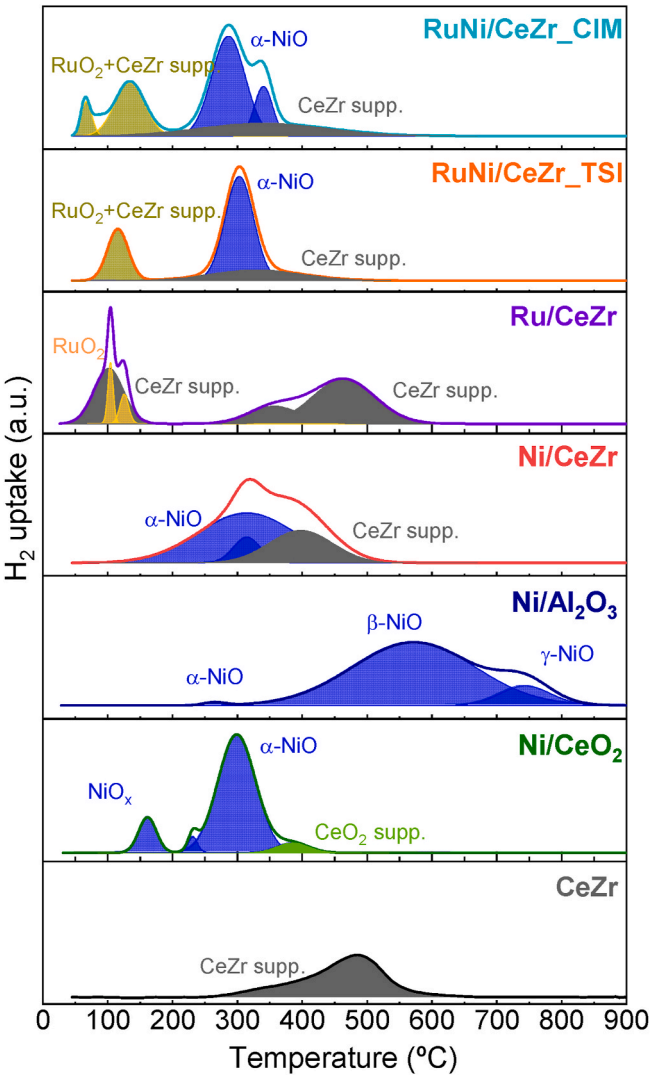

Fig. 3. TPR analysis results of the synthetized catalysts.

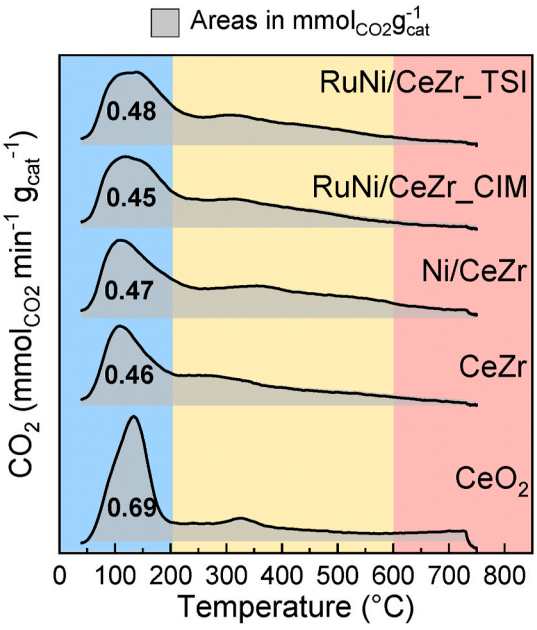

Fig. 4. CO_2-TPD analysis of all the catalysts and support employed in this work. The colored rectangles indicate the strongness of the basic sites being the blue, yellow and red areas the zones of weak, medium and strong sites, respectively. (For interpretation of the references to color in this figure legend, the reader is referred to the Web version of this article.)

formulation resulted in a marked enhancement of catalytic performance. Notably, improvements were observed in both activity and selectivity, with two distinct catalytic behaviors emerging.

For the co-impregnated RuNi/CeZr_CIM sample, the synergistic effect of the two metals facilitated catalyst activation at lower temperatures without significantly improving CO_2 conversion at temperatures above 350 °C. Furthermore, it exhibited significantly higher methane selectivity compared to the Ni/CeZr sample, resulting in an overall CH_4 yield (at similar conversions) that exceeded that of the monometallic formulation across the entire temperature range. In the case of the two-step impregnated RuNi/CeZr_TSI sample, both earlier catalyst activation and an enhanced CO_2 conversion were observed over the entire temperature range.

To provide a comprehensive overview of the catalytic performance of the studied samples, a comparative analysis with the most recent literature is presented in Table 3. This table highlights the results obtained under comparable reaction conditions (300 °C and 1 bar) and with similar catalyst formulations. As evidenced by the data, the methanation performances achieved with the formulations proposed in this study are highly competitive with those reported in the literature. Notably, our catalysts demonstrate excellent catalytic activity, even with relatively low active phase loadings and under high space velocity conditions.

This is particularly significant, as high SV often present a challenge to achieve both high CO_2 conversion and methane selectivity. Despite these conditions, our catalysts consistently displayed outstanding results, with CO_2 conversion and methane selectivity comparable to, or exceeding, those found in previous studies. This is especially remarkable given that many literature reports often rely on higher active phase loadings or operate at lower SV, which tend to promote higher conversion rates. Thus, the results of this study not only validate the effectiveness of the proposed catalyst formulations but also highlight their potential for industrial applications, where high space velocities and cost efficiency—achieved through lower active phase loadings—are essential.

The superior performance observed, particularly with Ni and Ru catalysts supported on ceria-zirconia ($Ce_{0.5}Zr_{0.5}$), underscores the crucial role of the synergistic interaction between the support and active metals in enhancing both methanation activity and selectivity, ensuring that these materials could be employed to renewable energy storage and grid integration scenarios. A commercial electrolyzer with 1 MW of capacity, typically produces 40–50 kg of H_2 per hour [31]. Using this input and considering the operating conditions and the results obtained in the present study, it could be possible to produce approximately 65 kg per day of methane (calculated with: stoichiometric ratio of the Sabatier reaction, i.e. calculating 220–275 kg of CO_2, and with 0.5 kg of RuNi/CeZr_TSI to ensure the 60 $NL(hg)^{-1}$ condition, and working at 350 °C). This level of methane production corresponds to 3607.5 MJ day^{-1} if burned or to 3575 MJ day^{-1} if used as stored energy (net useable energy after accounting for efficiencies losses).

3.3. Kinetic model

To better understand the role of the active species, the reaction kinetics were investigated. It is worth specifying that, even though it was not detailed in the experimental sections, the catalysts studied in this work demonstrated a remarkable stability overtime, with no sign of deactivation. The stability of this kind of formulations was addressed in a previous work [19]. For this reason, it was possible to perform the kinetic modelling analysis using the data obtained through the reported experiments, without the consideration of deactivation coefficients and

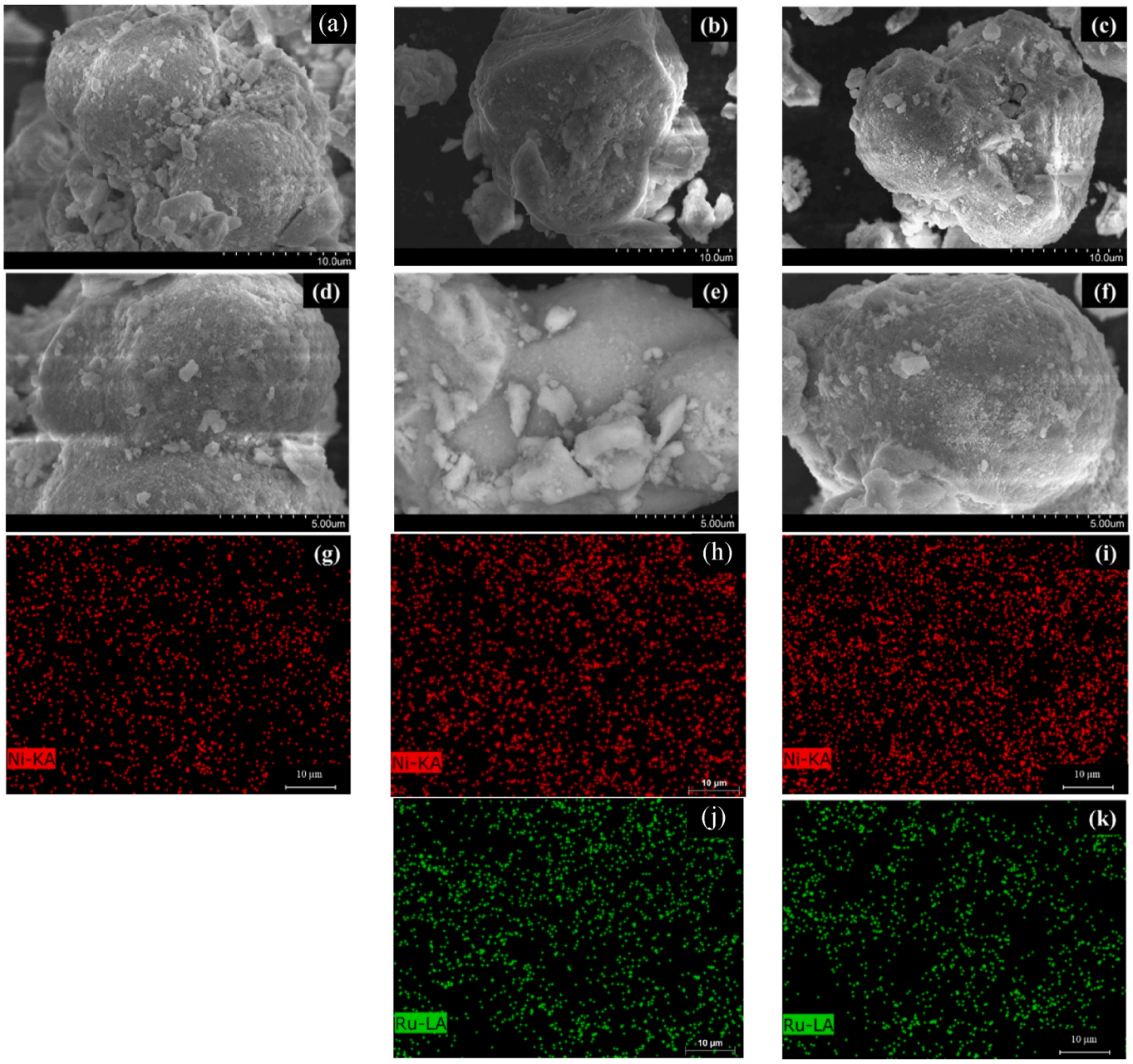

Fig. 5. SEM-EDX images for catalysts: (a), (d), (g) Ni/CeZr; (b), (e), (h), (j) RuNi/CeZr_TSI; (c), (f), (i), (k) RuNi/CeZr_CIM.

other mechanisms.

As discussed in section 2.4, the Xu and Froment model was employed to fit the experimental data. To investigate the reaction mechanism, the Arrhenius plots for each reaction and catalysts were compared (Fig. 8). Moreover, the exact values of the kinetic parameters (activation energy E_a and pre-exponential factor k_0) found for each reaction and catalyst are reported in Table 4.

To recall, k_1, k_2, and k_3 refers to the kinetic constant of CO methanation, reverse water-gas shift and direct CO_2 methanation, respectively. From Fig. 8a, it can be observed that all the nickel-based samples, both mono- and bimetallic, had a high activity toward the CO methanation reaction, reaching k_1 values higher than the Ru/CeZr catalyst. In addition, the reaction rate towards this reaction seemed to have a weak dependence on the operating temperature (at least in the investigated range) for the Ni-based catalysts, while a more evident temperature influence could be observed for the Ru/CeZr. The kinetic constant k_2 of the rWGS reaction seems to be even less affected by the temperature variation (Fig. 8b). Once again, the ruthenium catalyst demonstrated lower activity toward the reaction compared to the Ni-based catalysts, although the activity gap was significantly smaller than that observed for CO methanation. In summary, varying extents of the reverse water-gas shift (rWGS) reaction, indicated by CO production, were observed across all catalysts. The Sabatier reaction (Fig. 8c) showed a more evident dependence on the temperature for all the investigated formulations. The less active catalyst was the monometallic Ni/CeZr, while the monometallic ruthenium-based catalyst exhibited a reaction rate comparable to that of the bimetallic samples. This result is not surprising, since Ru is widely recognized as one of the best catalysts for CO_2 methanation [14].

According to the complex and detailed work carried out by Yaccato et al. [49], there are two possible mechanisms:

- CO_2 ← fast WGS equilibration → CO → CH_4
- CH_4 ← CO_2 ← WGS → CO → CH_4

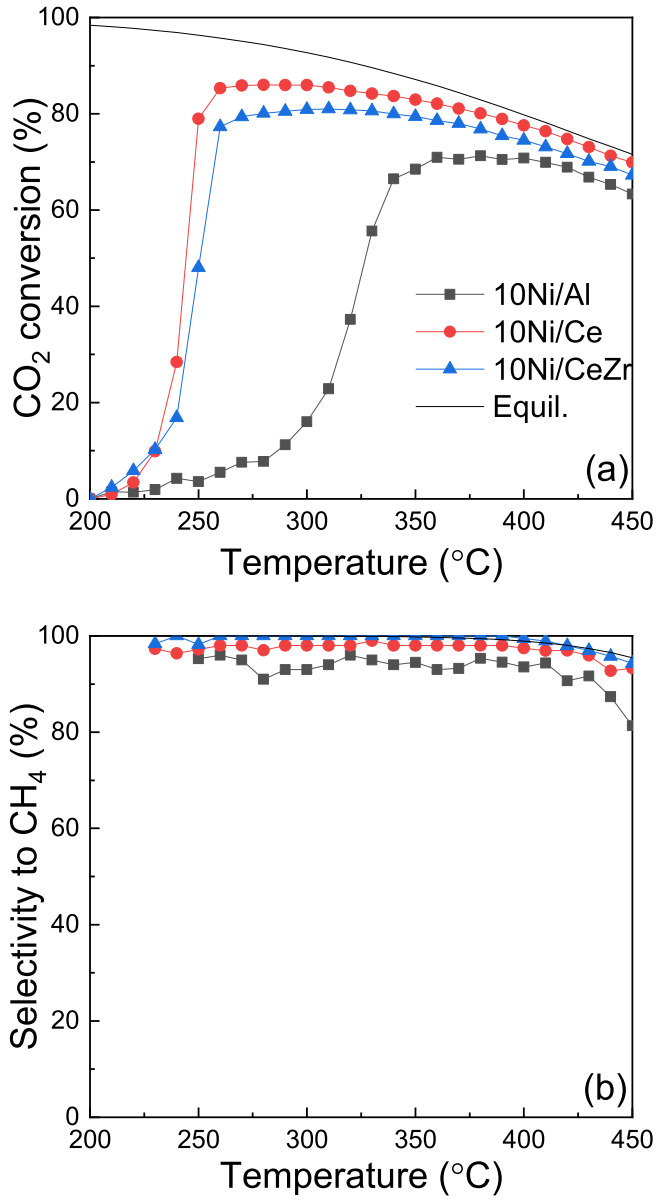

Fig. 6. CO_2 conversion and selectivity to methane for Ni/CeZr and benchmark catalysts. Operating conditions: P = 1 bar, SV = 30 NL(hg)$^{-1}$.

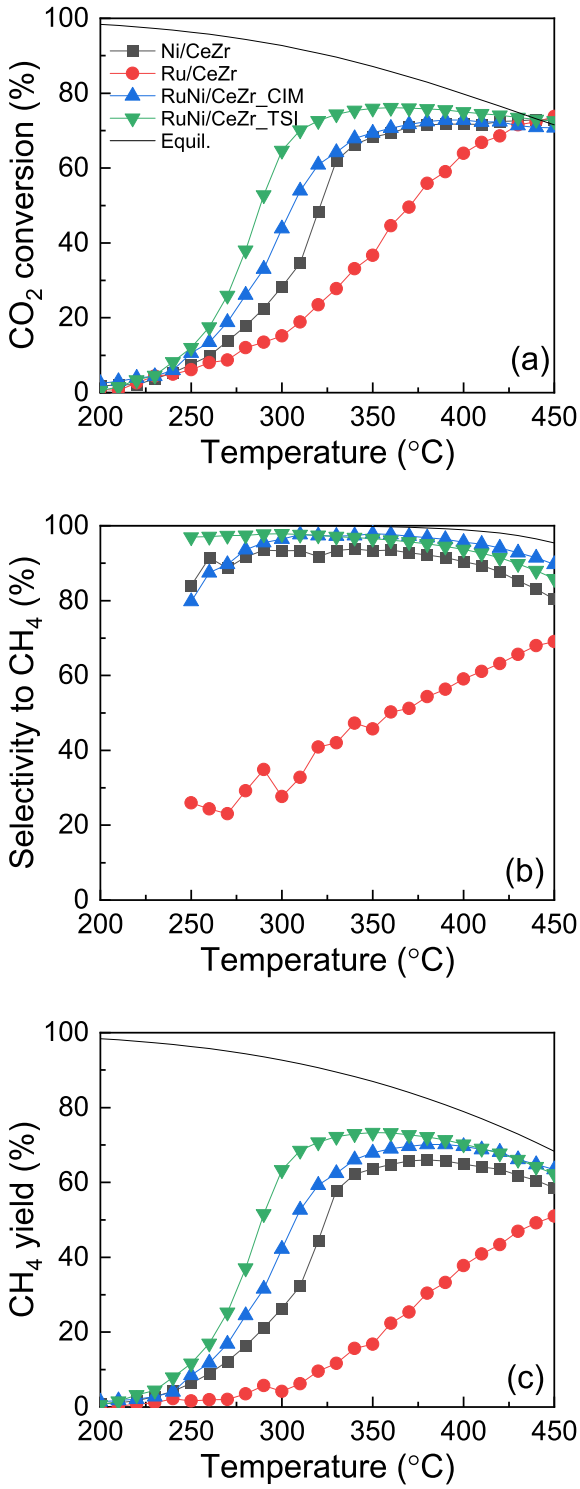

Fig. 7. CO_2 conversion, selectivity and yield to methane for CeZr supported mono- and bimetallic catalysts. Operating conditions: P = 1 bar, SV = 60 NL(hg)$^{-1}$.

In the first case, CO and CO_2 coexist and continuously shift, and CO hydrogenation is preferential. In the second configuration, methanation can occur equally from CO_2 and CO hydrogenation. The authors already suggested - observing a 1 % Ni catalyst - that methanation on nickel sites is "shift-assisted". The results of the present study, with a higher Ni-loaded catalysts, seems to corroborate this consideration. Indeed, hydrogenation of CO is few orders of magnitude higher than CO_2 (comparing Fig. 7a and c). On the other hand, ruthenium clearly follows the second proposed scheme, catalyzing in preferential order CO_2 hydrogenation > rWGS ≫ CO hydrogenation.

These observations can be sum-up in the reaction scheme proposed in Fig. 9.

Considering both the kinetic analysis and the catalytic test, the difference between the TSI sample and the CIM sample can be better understood. In case of RuNi/CeZr_CIM, a higher metal-metal interaction was suggested by TPR analysis, which could have hindered the maximization of CO_2 conversion. On the other hand, for RuNi/CeZr_TSI a lower interaction of the two metals was deducted by the TPR analysis, suggesting that Ru has a higher availability on the catalyst surface, being able to convert the maximum amount of CO_2 either to methane or carbon monoxide. Then, the proximity Ni-site further converts CO to methane, thus maximizing the methane yield. It is worth nothing that, according to this mechanism, CO formation was not inhibited. Hence, the selectivity towards methane was at its maximum when Ni-sites were able to further perform CO hydrogenation and dropped down at higher

Table 3
Literature review considering catalyst with similar composition tested at 300 °C and 1 bar under different SV.

Support	Active phase	SV	X_{CO2}	S_{CH4}	Ref.
		NL $(hg)^{-1}$	%	%	
Al_2O_3	25 %Ni–20 %Ce	40	68	100	[32]
Al_2O_3	25 %Ni–5 %Ce	9	72	98	[33]
Al_2O_3	25 %Ni–5 %Zr	9	15	100	
Ce	0.4 %Ru–4 %Ni	40	45	100	[34]
$Ni_{80}Ce_4Y_{20}$	1 %Ru	18	80	100	[35]
$Ni_{0.73}Zr_{0.03}Al_{0.24}$		15	95	98	[36]
ZrO_2	66 mol.%	24	70	98	[37]
ZrO_2	20 %Ni	48	90	100	[38]
Zr_x-SBA15	10 %Ni	45	35	100	[39]
0.15Zr-CeO_2	15 %Ni	12	80	100	[40]
$Ce_{0.8}Zr_{0.2}$-MOF	20 %Co_3O_4	15	70	98	[41]
$Ce_{0.5}Zr_{0.5}$	15 %Ni–1 %Ru	24	40	100	[42]
$Ce_{0.8}Zr_{0.2}$	Ni	20	20	100	[43]
$Ce_{0.2}Zr_{0.8}$-MOF	10 %Ni (one-pot)	24	50	100	[44]
$Ce_{0.8}Zr_{0.2}$	15 %Ni	12	60	98	[45]
$Pr_{0.1}Ce_{0.9}$	1 %Ru–10 %Ni	25	80	100	[14]
$Ce_{0.25}Zr_{0.75}$	45 %Ni	a	30	100	[46]
$Ce_{0.8}Zr_{0.2}O_2$	10 %Ni	12	80	99	[47]
CNF	16 %Ni	96	22	96	[13]
HNTs	17 %Ni	7.5	96	97	[48]
$Ce_{0.5}Zr_{0.5}$	10 %Ni	30	82	100	**This work**
$Ce_{0.5}Zr_{0.5}$	10 %Ni	60	30	92	**This work**
$Ce_{0.5}Zr_{0.5}$	0.5 %Ru	60	17	25	**This work**
$Ce_{0.5}Zr_{0.5}$	0.5 %Ru–10 %Ni (CIM)	60	48	98	**This work**
$Ce_{0.5}Zr_{0.5}$	0.5 %Ru/10 %Ni (TSI)	60	69	98	**This work**

[a] SV not indicated.

temperature when the approach to the thermodynamic equilibrium became more significant.

4. Conclusions

This study was devoted to the experimental evaluation of the activity of Ni- and Ru- based ceria-zirconia supported catalysts, and to the elucidation of the role of each component of the formulation on the reaction kinetics. To this aim, a Ni/CeZr sample was prepared and compared to more conventional CeO_2- and Al_2O_3- supported catalysts; then, mono- and bimetallic catalysts containing Ru were prepared and tested.

The mixed oxide CeZr employed as support for Ni-based catalysts demonstrated only slight differences in terms of catalytic performances compared to CeO_2, while it was remarkably more active than alumina. The prepared Ni/CeZr catalyst is, however, competitive compared to other literature formulations. Ruthenium addition to Ni/CeZr allows to enhance the methane yield, although Ru alone had scarce performances at the investigated high space velocities. Different interactions are established by variating the catalysts preparation method: the techniques that allowed to obtain more free ruthenium onto the catalyst surface achieved the best results. The efficiency of the catalytic formulation is correlated to the balance between the three characteristic reactions of the system; in bimetallic catalysts, a high ratio between a CO activating metal and CO_2 activating metal can be beneficial to obtain high selectivity. By advancing the understanding of catalyst design for CO_2 methanation, this work contributes to the development of efficient PtG processes, which are essential for large-scale renewable energy storage and carbon utilization. These insights help bridge the gap between laboratory research and industrial deployment, facilitating the integration of renewable energy into existing infrastructure and supporting global decarbonization goals performance of methanation catalysts is critical for the efficiency and scalability of PtG systems.

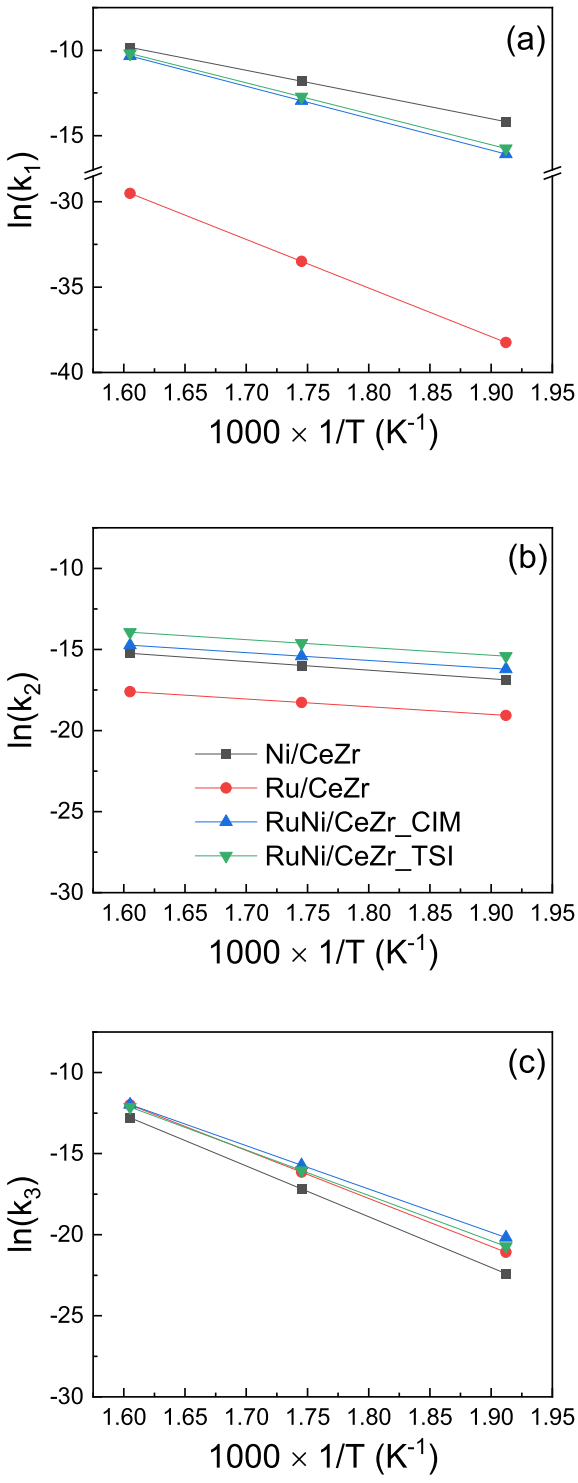

Fig. 8. Arrhenius plot for the analysis.

Building upon the promising results obtained in this study, future work should focus on two main directions. First, a deeper investigation of the Ce:Zr ratio in the support material could provide valuable insights into the role of surface oxygen mobility, basicity, and metal–support interactions in enhancing catalytic performance. In addition, tailoring the Ce:Zr composition may allow for further optimization of dispersion, reducibility, and the stabilization of active metal species. Second, the

Table 4
Kinetic parameters.

	CO methanation		r-WGS		Sabatier reac.		R^2
	k_0	E_a	k_0	E_a	k_0	E_a	
Ni/CeZr	4.14×10^5	138	1.23×10^{-3}	44	1.90×10^{16}	260	0.92
Ru/CeZr	10.9×10^7	237	4.95×10^{-5}	40	2.63×10^{15}	246	0.94
RuNi/ CeZr_CIM	3.68×10^8	156	8.71×10^{-4}	40	2.59×10^{13}	222	0.90
RuNi/ CeZr_TSI	1.58×10^8	151	2.01×10^{-4}	40	1.87×10^{14}	233	0.91

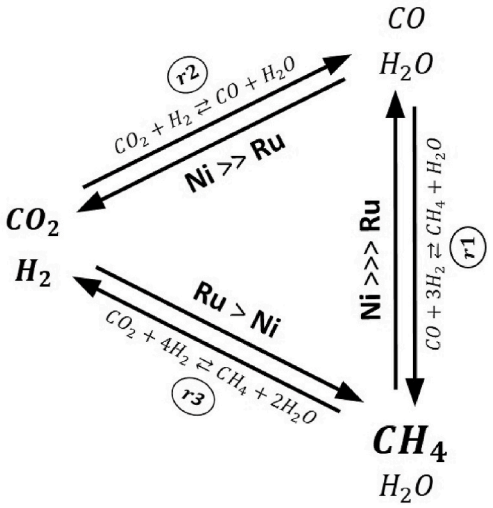

Fig. 9. Proposed reaction-catalysts scheme.

kinetic model developed under lab-scale conditions should be validated at higher technology readiness levels (TRLs) through scale-up experiments. Testing the most active formulations, such as RuNi/CeZr_TSI, under conditions closer to industrial operation (e.g., higher space velocities and extended time-on-stream) would allow for assessing the robustness of the observed reaction mechanisms and the applicability of the kinetic parameters at larger scales. This approach is essential for bridging the gap between fundamental research and practical implementation in Power-to-Gas systems, where catalyst stability, performance under dynamic loads, and process integration become critical factors.

These developments will contribute to a more comprehensive understanding of CO_2 methanation over advanced CeZr-supported catalysts and support their transition toward industrial deployment in renewable energy storage and carbon utilization technologies.

CRediT authorship contribution statement

Antonio Ricca: Methodology, Investigation, Formal analysis, Conceptualization. **Simona Renda:** Writing – review & editing, Writing – original draft, Visualization, Validation, Investigation, Formal analysis, Data curation. **Christian Di Stasi:** Writing – review & editing, Writing – original draft, Visualization, Validation, Investigation, Formal analysis, Data curation. **Livia Truda:** Investigation. **Vincenzo Palma:** Supervision, Project administration.

Declaration of competing interest

The authors declare that they have no known competing financial interests or personal relationships that could have appeared to influence the work reported in this paper.

Acknowledgments

C.D.S. and S.R. are grateful to Dr. José Luis Pinilla and Dr. Isabel Suelves for the aid and the support provided to this work. C.D.S is grateful for the Juan de la Cierva (JdC) fellowship (Grant Number: JDC2022-048765-I) funded by MICIU/AEI /10.13039/501100011033 and by the European Union NextGenerationEU/PRTR. S.R. acknowledges the funding of the Juan de la Cierva fellowship (grant no. JDC2023-052947-I) by MCIU/AEI/10.13039/501100011033 and FSE+. The authors acknowledge the Analysis and Characterization service at ICB-CSIC.

References

[1] S. Renda, J. Soler, J. Herguido, M. Menéndez, Effect of particles size and density on the segregation of catalyst-sorbent mixtures for direct sorption-enhanced DME synthesis: experimental and mathematical study, Biomass Bioenergy 197 (2025), https://doi.org/10.1016/j.biombioe.2025.107764.
[2] L. Guo, T. Zhang, J. Qiu, J. Bai, Z. Li, H. Wang, X. Cai, Y. Yang, Y. Xu, Cobalt-doped Ni-based catalysts for low-temperature CO2 methanation, Renew. Energy 236 (2024) 121512, https://doi.org/10.1016/J.RENENE.2024.121512.
[3] C. Di Stasi, S. Renda, G. Greco, B. González, V. Palma, J.J. Manyà, Wheat-straw-derived activated biochar as a renewable support of ni-ceo2 catalysts for co2 methanation, Sustainability 13 (2021), https://doi.org/10.3390/su13168939.
[4] D. Sprake, Y. Vagapov, S. Lupin, A. Anuchin, Housing estate energy storage feasibility for a 2050 scenario, in: 2017 Internet Technologies and Applications, ITA 2017 - Proceedings of the 7th International Conference, Institute of Electrical and Electronics Engineers Inc., 2017, pp. 137–142, https://doi.org/10.1109/ITECHA.2017.8101925.
[5] J. Ren, H. Lou, N. Xu, F. Zeng, G. Pei, Z. Wang, Methanation of CO/CO2 for power to methane process: fundamentals, status, and perspectives, J. Energy Chem. 80 (2023) 182–206, https://doi.org/10.1016/J.JECHEM.2023.01.034.
[6] S. Chen, A.M. Abdel-Mageed, Methanation reactions for chemical storage and purification of hydrogen: overview and structure-reactivity correlations in supported metals, Int. J. Hydrogen Energy 48 (2023) 24915–24935, https://doi.org/10.1016/J.IJHYDENE.2022.12.196.
[7] M. Thema, F. Bauer, M. Sterner, Power-to-Gas: electrolysis and methanation status review, Renew. Sustain. Energy Rev. 112 (2019) 775–787, https://doi.org/10.1016/J.RSER.2019.06.030.
[8] A. Beniwal, A. Bagaria, T.Y. Chen, D. Bhalothia, Advancements in CO2 conversion technologies: a comprehensive review on catalyst design strategies for high-performance CO2 methanation, Sustain. Energy Fuels 9 (2025) 2261–2286, https://doi.org/10.1039/d5se00167f.
[9] C. Wang, H. Sun, X. Liu, X. Jin, Y. Feng, H. Shi, D. Wang, Y. Zhang, Y. Wang, Z. Yan, Low-temperature CO2 methanation over Ru/CeO2: investigation into Ru loadings, Fuel 345 (2023), https://doi.org/10.1016/j.fuel.2023.128238.
[10] I. Iglesias, A. Quindimil, F. Mariño, U. De-La-Torre, J.R. González-Velasco, Zr promotion effect in CO 2 methanation over ceria supported nickel catalysts, Int. J. Hydrogen Energy 44 (2019) 1710–1719, https://doi.org/10.1016/j.ijhydene.2018.11.059.
[11] F. Ocampo, B. Louis, L. Kiwi-Minsker, A.C. Roger, Effect of Ce/Zr composition and noble metal promotion on nickel based CexZr1−xO2 catalysts for carbon dioxide methanation, Appl. Catal. Gen. 392 (2011) 36–44, https://doi.org/10.1016/J.APCATA.2010.10.025.
[12] Y. Peng, X.L. Si, C. Shang, Z.P. Liu, Abundance of low-energy oxygen vacancy pairs dictates the catalytic performance of cerium-stabilized zirconia, J. Am. Chem. Soc. 146 (2024) 10822–10832, https://doi.org/10.1021/jacs.4c01285.
[13] C. Di Stasi, J. López-de los Ríos, A. Ayala-Cortés, D. Torres, J.L. Pinilla, I. Suelves, Activity enhancement of carbon nanofiber-based catalysts for CO2 methanation by mechanochemical synthesis, J. CO2 Util. 89 (2024) 102965, https://doi.org/10.1016/J.JCOU.2024.102965.
[14] A.I. Tsiotsias, N.D. Charisiou, C. Italiano, G.D. Ferrante, L. Pino, A. Vita, V. Sebastian, S.J. Hinder, M.A. Baker, A. Sharan, N. Singh, K. Polychronopoulou, M.A. Goula, Ni-noble metal bimetallic catalysts for improved low temperature CO2 methanation, Appl. Surf. Sci. 646 (2024) 158945, https://doi.org/10.1016/J.APSUSC.2023.158945.
[15] L.H. Vieira, L.F. Rasteiro, C.S. Santana, G.L. Catuzo, A.H.M. da Silva, J.M. Assaf, E. M. Assaf, Noble metals in recent developments of heterogeneous catalysts for CO2 conversion processes, ChemCatChem 15 (2023), https://doi.org/10.1002/cctc.202300493.
[16] E. Ifandi, D.T.C. Lai, S. Kalaitzidis, M.S. Abu Bakar, T. Grammatikopoulos, C.K. Lai, B. Tsikouras, Noble metal catalyst detection in rocks using machine-learning: the future to low-cost, green energy materials? Sci. Rep. 13 (2023) https://doi.org/10.1038/s41598-023-30822-6.
[17] X. Gao, C.R. Chang, Characterizing the sequential effects toward the impregnations of supported bimetallic catalysts, Mol. Catal. 527 (2022) 112411, https://doi.org/10.1016/J.MCAT.2022.112411.
[18] M.C. Ozcan, P. Degirmencioglu, E.E.B.P. Karaman, K. Murtezaoglu, N. Oktar, Effect of the amount and type of active metal and its impregnation sequence on bio-fuel production, Appl. Catal. Gen. 683 (2024) 119850, https://doi.org/10.1016/J.APCATA.2024.119850.

[19] S. Renda, A. Ricca, V. Palma, Precursor salts influence in Ruthenium catalysts for CO2 hydrogenation to methane, Appl. Energy 279 (2020), https://doi.org/10.1016/j.apenergy.2020.115767.
[20] J. Xu, G.F. Froment, Methane steam reforming, methanation and water-gas shift: I. Intrinsic kinetics, AIChE J. 35 (1989) 88–96, https://doi.org/10.1002/aic.690350109.
[21] R.-Y. Chein, C.-T. Yu, C.-C. Wang, Numerical simulation on the effect of operating conditions and syngas compositions for synthetic natural gas production via methanation reaction, Fuel 185 (2016) 394–409, https://doi.org/10.1016/j.fuel.2016.07.123.
[22] S. Renda, M. Martino, V. Palma, CO2 methanation over open cell foams prepared via chemical conversion coating, J. Clean. Prod. 434 (2024), https://doi.org/10.1016/j.jclepro.2023.140221.
[23] D. Freidzon, O. Kraynis, E. Wachtel, I. Lubomirsky, T. Livneh, The elastic component of anisotropic strain dominates the observed shift in the F2g Raman mode of anelastic ceria thin films, Phys. Chem. Chem. Phys. 25 (2023) 30563–30571, https://doi.org/10.1039/d3cp03878e.
[24] S. Chang, M. Li, Q. Hua, L. Zhang, Y. Ma, B. Ye, W. Huang, Shape-dependent interplay between oxygen vacancies and Ag-CeO 2 interaction in Ag/CeO 2 catalysts and their influence on the catalytic activity, J. Catal. 293 (2012) 195–204, https://doi.org/10.1016/j.jcat.2012.06.025.
[25] B. Azambre, L. Zenboury, A. Koch, J.V. Weber, Adsorption and desorption of NOx on commercial ceria-zirconia (Ce xZr1-xO2) mixed oxides: a combined TGA, TPD-MS, and DRIFTS study, J. Phys. Chem. C 113 (2009) 13287–13299, https://doi.org/10.1021/jp9008674.
[26] M. Gil-Calvo, C. Jiménez-González, B. De Rivas, J.I. Gutiérrez-Ortiz, R. López-Fonseca, Novel nickel aluminate-derived catalysts supported on ceria and ceria-zirconia for partial oxidation of methane, Ind. Eng. Chem. Res. 56 (2017) 6186–6197, https://doi.org/10.1021/acs.iecr.7b00986.
[27] R. Molina, G. Poncelet, α-Alumina-Supported Nickel Catalysts Prepared from Nickel Acetylacetonate: a TPR Study, 1998.
[28] C. Pizzolitto, F. Menegazzo, E. Ghedini, G. Innocenti, A. Di Michele, G. Cruciani, F. Cavani, M. Signoretto, Increase of Ceria redox ability by lanthanum addition on Ni based catalysts for hydrogen production, ACS Sustain. Chem. Eng. 6 (2018) 13867–13876, https://doi.org/10.1021/acssuschemeng.8b02103.
[29] S.D. Dhas, P.S. Maldar, M.D. Patil, A.B. Nagare, M.R. Waikar, R.G. Sonkawade, A. V. Moholkar, Synthesis of NiO nanoparticles for supercapacitor application as an efficient electrode material, Vacuum 181 (2020) 109646, https://doi.org/10.1016/J.VACUUM.2020.109646.
[30] J. Zhang, Z.C. Kang, L. Eyring, The binary higher oxides of the rare earths, J. Alloys Compd. 192 (1993) 57–63, https://doi.org/10.1016/0925-8388(93)90186-Q.
[31] A. Al-Douri, K.M. Groth, Hydrogen production via electrolysis: state-of-the-art and research needs in risk and reliability analysis, Int. J. Hydrogen Energy 63 (2024) 775–785, https://doi.org/10.1016/J.IJHYDENE.2024.03.188.
[32] A. Alarcón, J. Guilera, J.A. Díaz, T. Andreu, Optimization of nickel and ceria catalyst content for synthetic natural gas production through CO2 methanation, Fuel Process. Technol. 193 (2019) 114–122, https://doi.org/10.1016/j.fuproc.2019.05.008.
[33] R. Daroughegi, F. Meshkani, M. Rezaei, Enhanced low-temperature activity of CO2 methanation over ceria-promoted Ni-Al2O3 nanocatalyst, Chem. Eng. Sci. 230 (2021), https://doi.org/10.1016/j.ces.2020.116194.
[34] N. Elia, J. Estephane, C. Poupin, B. El Khoury, L. Pirault-Roy, S. Aouad, E.A. Aad, A highly selective and stable ruthenium-nickel supported on ceria catalyst for carbon dioxide methanation, ChemCatChem 13 (2021) 1559–1567, https://doi.org/10.1002/cctc.202001687.
[35] Q. Ye, S. Li, Y. Liao, Y. Wang, Y. He, J. Chen, J. Xu, Q. Su, X. Cui, Ce enhanced RuNi alloy multi-metal synergic hydrotalcite oxide derived catalyst for high performance CO2 methanation, Chem. Eng. J. 486 (2024), https://doi.org/10.1016/j.cej.2024.150426.
[36] F. He, J. Zhuang, B. Lu, X. Liu, J. Zhang, F. Gu, M. Zhu, J. Xu, Z. Zhong, G. Xu, F. Su, Ni-based catalysts derived from Ni-Zr-Al ternary hydrotalcites show outstanding catalytic properties for low-temperature CO2 methanation, Appl. Catal., B 293 (2021), https://doi.org/10.1016/j.apcatb.2021.120218.
[37] M. Zhang, J. Ye, Y. Qu, X. Lu, K. Luo, J. Dong, N. Lu, Q. Niu, P. Zhang, S. Dai, Highly stable and selective Ni/ZrO2 nanofiber catalysts for efficient CO2 methanation, ACS Appl. Mater. Interfaces 16 (2024) 34936–34946, https://doi.org/10.1021/acsami.4c04124.
[38] H. Fu, S. Sun, H. Lian, Enhanced low-temperature CO2 methanation over Ni/ZrO2-Al2O3catalyst: effect of Al addition on catalytic performance and reaction mechanism, J. CO2 Util. 69 (2023), https://doi.org/10.1016/j.jcou.2023.102415.
[39] R. Tang, N. Ullah, Z. Li, Unveiling the promotion effect of Zr species on SBA-15 supported nickel catalysts for CO2 methanation, Int. J. Hydrogen Energy 48 (2023) 4694–4707, https://doi.org/10.1016/j.ijhydene.2022.11.011.
[40] N. Tri, N. Phung Anh, D. Ba Long, H. Gia Thien Thanh, B. Thi Hong Nhung, N. Thi Thuy Van, C. Anh Ha, H. Tien Cuong, L. Cam Loc, Advanced Zr-CeO2 supported Ni catalysts for production of synthetic natural gas (SNG) from CO2, Fuel 380 (2025), https://doi.org/10.1016/j.fuel.2024.133137.
[41] D. Jampaiah, D. Damma, A. Chalkidis, P. Venkataswamy, S.K. Bhargava, B. M. Reddy, MOF-derived ceria-zirconia supported Co3O4 catalysts with enhanced activity in CO2 methanation, Catal. Today 356 (2020) 519–526, https://doi.org/10.1016/j.cattod.2020.05.047.
[42] L.P. Merkouri, E. le Saché, L. Pastor-Pérez, M.S. Duyar, T. Ramirez Reina, Versatile Ni-Ru catalysts for gas phase CO2 conversion: bringing closer dry reforming, reverse water gas shift and methanation to enable end-products flexibility, Fuel 315 (2022), https://doi.org/10.1016/j.fuel.2021.123097.
[43] Y. Yu, Z. Bian, Z. Wang, J. Wang, W. Tan, Q. Zhong, S. Kawi, CO2 methanation on Ni-Ce0.8M0.2O2 (M=Zr, Sn or Ti) catalyst: suppression of CO via formation of bridging carbonyls on nickel, Catal. Today 424 (2023), https://doi.org/10.1016/j.cattod.2020.07.049.
[44] S. Liu, X. Feng, J.X. Xu, J. Wang, Y. Zhao, H. Wang, Q. Zhang, A research on the synthesis process of Zr-MOF derived Ni-based catalysts for CO2 methanation: the role of Ce promoter, method of Ni introduction and calcination condition, Fuel 379 (2025), https://doi.org/10.1016/j.fuel.2024.132962.
[45] L. Xu, X. Wen, M. Chen, C. Lv, Y. Cui, X. Wu, C.e. Wu, B. Yang, Z. Miao, X. Hu, Mesoporous Ce-Zr solid solutions supported Ni-based catalysts for low-temperature CO2 methanation by tuning the reaction intermediates, Fuel 282 (2020), https://doi.org/10.1016/j.fuel.2020.118813.
[46] A. Traitangwong, X. Guo, V. Meeyoo, C. Li, XNi/Ni0.05Ce0.20Zr0.75O2Solid solution over a CO2Methanation reaction, Ind. Eng. Chem. Res. 59 (2020) 13440–13449, https://doi.org/10.1021/acs.iecr.0c01526.
[47] B. Chen, J. Qiu, L. Xu, Y. Cui, Ni-based mesoporous Ce0.8Zr0.2O2 catalyst with enhanced low-temperature performance for CO2 methanation, Catal. Commun. 171 (2022) 106515, https://doi.org/10.1016/J.CATCOM.2022.106515.
[48] D. Yang, X. Meng, B. Xu, D. Jin, W. Dai, R. Zhao, F. Xu, Z. Xin, Nitric acid-pretreated natural halloysite nanotubes as Ni nanoparticle catalyst supports for CO2 methanation, ACS Appl. Nano Mater. 7 (2024) 2190–2199, https://doi.org/10.1021/ACSANM.3C05492.
[49] K. Yaccato, R. Carhart, A. Hagemeyer, A. Lesik, P. Strasser, A.F. Volpe, H. Turner, H. Weinberg, R.K. Grasselli, C. Brooks, Competitive CO and CO2 methanation over supported noble metal catalysts in high throughput scanning mass spectrometer, Appl. Catal. Gen. 296 (2005) 30–48, https://doi.org/10.1016/j.apcata.2005.07.052.